



Universiteit
Leiden
The Netherlands

A nondetection of Iron in the first high-resolution emission study of the lava planet 55 Cnc e

Rasmussen, K.C.; Currie, M.H.; Hagee, C.; Buchem, C.P.A. van; Malik, M.; Savel, A.B.; ... ; Bean, J.L.

Citation




















Rasmussen, K. C., Currie, M. H., Hagee, C., Buchem, C. P. A. van, Malik, M., Savel, A. B., ... Bean, J. L. (2023). A nondetection of Iron in the first high-resolution emission study of the lava planet 55 Cnc e. *The Astronomical Journal*, 166(4). doi:10.3847/1538-3881/acf28e

Version: Publisher's Version
License: [Creative Commons CC BY 4.0 license](https://creativecommons.org/licenses/by/4.0/)
Downloaded from: <https://hdl.handle.net/1887/3716573>

Note: To cite this publication please use the final published version (if applicable).



A Nondetection of Iron in the First High-resolution Emission Study of the Lava Planet 55 Cnc e

Kaitlin C. Rasmussen^{1,2,16} , Miles H. Currie^{1,2,16} , Celeste Hagee³ , Christiaan van Buchem^{4,5} , Matej Malik⁶ ,
Arjun B Savel⁶, Matteo Brogi^{7,8,9} , Emily Rauscher¹⁰ , Victoria Meadows^{1,2} , Megan Mansfield^{11,17} ,
Eliza M.-R. Kempton⁶ , Jean-Michel Desert¹² , Joost P. Wardenier¹³ , Lorenzo Pino¹⁴ , Michael Line¹¹ ,
Vivien Parmentier¹³ , Andreas Seifahrt¹⁵ , David Kasper¹⁵ , Madison Brady¹⁵ , and Jacob L. Bean¹⁵ 

¹ Department of Astronomy and Astrobiology Program, University of Washington, Box 351580, Seattle, WA 98195, USA
² NASA Nexus for Exoplanet System Science, Virtual Planetary Laboratory Team, Box 351580, University of Washington, Seattle, WA 98195, USA

³ Department of Astronomy, University of Washington, Seattle, WA 98195, USA

⁴ University of Leiden, The Netherlands

⁵ Vrije Universiteit Amsterdam, The Netherlands

⁶ Department of Astronomy, University of Maryland, College Park, MD 20742, USA

⁷ Department of Physics, University of Warwick, Coventry CV4 7AL, UK

⁸ INAF—Osservatorio Astrofisico di Torino, Via Osservatorio 20, I-10025, Pino Torinese, Italy

⁹ Centre for Exoplanets and Habitability, University of Warwick, Gibbet Hill Road, Coventry CV4 7AL, UK

¹⁰ Department of Astronomy and Astrophysics, University of Michigan, Ann Arbor, MI 48109, USA

¹¹ Steward Observatory, University of Arizona, Tucson, AZ 85719, USA

¹² Anton Pannekoek Institute of Astronomy, University of Amsterdam, P.O. Box 94249, 1090GE Amsterdam, Noord Holland, The Netherlands

¹³ Department of Physics (Atmospheric, Oceanic and Planetary Physics), University of Oxford, Oxford, OX1 3PU, UK

¹⁴ INAF—Osservatorio Astrofisico di Arcetri, Firenze, Italy

¹⁵ Department of Astronomy & Astrophysics, University of Chicago, Chicago, IL, USA

Received 2023 May 1; revised 2023 August 11; accepted 2023 August 20; published 2023 September 12

Abstract

Close-in lava planets represent an extreme example of terrestrial worlds, but their high temperatures may allow us to probe a diversity of crustal compositions. The brightest and most well-studied of these objects is 55 Cancri e, a nearby super-Earth with a remarkably short 17 hr orbit. However, despite numerous studies, debate remains about the existence and composition of its atmosphere. We present upper limits on the atmospheric pressure of 55 Cnc e derived from high-resolution time-series spectra taken with Gemini-N/MAROON-X. Our results are consistent with current crustal evaporation models for this planet which predict a thin ~ 100 mbar atmosphere. We conclude that, if a mineral atmosphere is present on 55 Cnc e, the atmospheric pressure is below 100 mbar.

Unified Astronomy Thesaurus concepts: [Exoplanet atmospheres \(487\)](#); [Observational astronomy \(1145\)](#)

1. Introduction

Lava planets—worlds whose equilibrium temperatures are so high that a significant portion of their crust is molten—represent the extreme in the canon of rocky terrestrial planets. 55 Cancri e (McArthur et al. 2004) is a canonical lava planet. It is a super-Earth with a mass of $8.63 M_{\oplus}$ and density of 6.66 g cm^{-3} , comparable to, but higher than Earth's 5.5 g cm^{-3} . It has a radius of $2.00 R_{\oplus}$ and a period of just 0.736 day (Bourrier et al. 2018; Crida et al. 2018). Spitzer phase curves suggest that 55 Cnc e is synchronously rotating (Hammond & Pierrehumbert 2018), with two different dayside brightness temperatures reported: Demory et al. (2016) reports that this value is 2700^{+270}_{-270} K at $4.5 \mu\text{m}$; a recent reanalysis performed by Mercier et al. (2022) finds it to be 3771^{+665}_{-590} ; Demory et al. (2016) found a relatively large hotspot offset (which can indicate the presence of an advected atmosphere) of 41^{+12}_{-12} degrees in longitude; while the reanalysis of Mercier et al. (2022) indicates a smaller hotspot offset of -12^{+21}_{-18} degrees.

In the last several years, many studies have used transmission spectroscopy to search for the presence and nature of 55 Cnc e's atmosphere, with the growing consensus pointing toward a higher likelihood for either a high molecular weight atmosphere or no atmosphere. Initial support for 55 Cnc e having a low mean molecular weight atmosphere, came from Tsiaras et al. (2016) who used Hubble Space Telescope/WFC3 data to infer a hydrogen-rich atmosphere and a tentative detection of HCN. Esteves et al. (2017) also found transmission signatures consistent with either an H_2 -dominated, or high mean molecular weight atmosphere with H_2O , or terminator clouds. However, subsequent observations failed to support the presence of an H_2 -dominated atmosphere, with Deibert et al. (2021) using nondetections to place low constraints on HCN, NH_3 , and C_2H_2 ; and Zhang et al. (2021) failing to detect the expected escaping He. Bourrier et al. (2018) also argued against the presence of an H/He envelope based on the bulk density and radius of the planet, and concluded that a high molecular weight atmosphere was likely present, in agreement with the results of Demory et al. (2016) and Angelo & Hu (2017). Jindal et al. (2020) subsequently used Gemini-N/GRACES and a sensitive nondetection of TiO and water, to rule out low molecular weight or clear-sky water-rich atmospheres, although the results were also consistent with cloudy or no atmosphere. Ridden-Harper et al. (2016) and Keles et al. (2022) both used high-resolution transmission spectroscopy to search for traces of a mineral atmosphere but found none.

¹⁶ cofirst author.

¹⁷ NHFP Sagan Fellow.



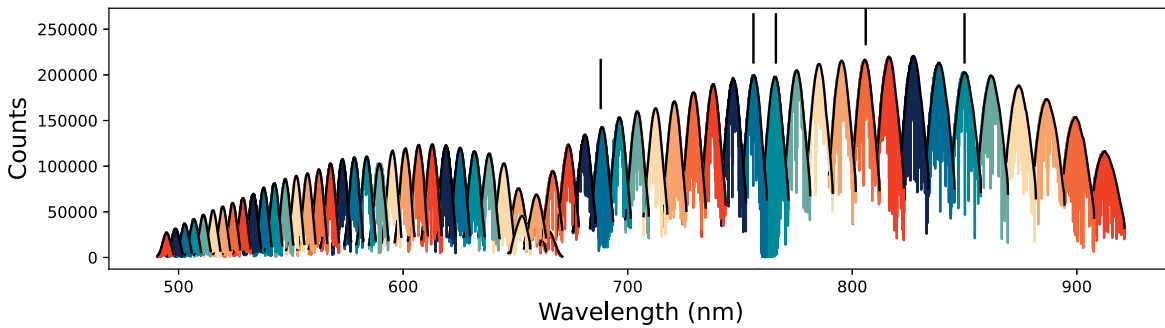


Figure 1. One full set of echelle orders for one spectrum. The y-axis is raw counts. The x-axis is wavelength in nm. The blue S/N is ~ 260 and the red S/N is ~ 370 . The orders indicated by the black lines were removed for having saturated lines or containing tellurics.

Photometry has also been used to understand 55 Cnc e’s thermal emission and search for signs of an atmosphere. Winn et al. (2011) used the Microvariability and Oscillations of STars (MOST; Rucinski et al. 2003) satellite to discover an unexplained IR phase modulation (i.e., a change in the sinusoidal brightness function associated with the changing phase) too large to be caused by combined star-planet fluctuations in brightness. Later, Sulis et al. (2019) used MOST to confirm that the thermal emission of the planet was variable through time. The IR Spitzer results from Demory et al. (2016) suggested that 55 Cnc e has either an optically thick atmosphere, or surface magma flow. However, a second analysis of the Spitzer phase curves found a higher dayside temperature at $4.5 \mu\text{m}$, which was interpreted as emission from a temperature inversion generated in an atmosphere of UV-absorbing SiO vapor (Mercier et al. 2022).

Signatures of crustal evaporation in particular is an intriguing avenue of exploration for 55 Cnc e because of the predicted detectability of evaporated species such as sodium, silicate oxide, potassium, oxygen, iron, and magnesium (Ito et al. 2015, 2022). At significant enough rates of evaporation, minerals with strong features in the optical spectrum should appear at the 10^{-4} planet-to-star contrast ratio, a level observable by a large ground-based telescope equipped with a high-resolution spectrograph. Additionally, SiO and SiO₂ features may be detectable with the MIRI instrument on JWST (Zilinskas et al. 2022).

Here we present an informative nondetection of gaseous iron in 55 Cnc e with optical dayside emission spectroscopy. In Section 2, we discuss the observation and modeling of the planet. In Section 3, we describe our cross-correlation methodology and signal smearing mitigation strategy. In Section 4, we present our results.

2. Data and Models

Spectroscopic data were obtained at $R \sim 85,000$ with the MAROON-X optical spectrograph on Gemini-North (Seifahrt et al. 2016, 2018, 2020, 2022). The observation began at 07:48 UTC on 2022 March 27, and ended at 11:12 UTC. The planned exposure time for each frame was 130 s; however, the seeing on Maunakea was below average ($\sim 0.7''$), prompting us to increase our exposure time to 300 s per frame for each of the 31 total frames we observed. The mean signal-to-noise ratio (S/N) of the blue frames was 260 and the mean S/N of the red frames was 370, as shown in Figure 1. We began the observation just after secondary eclipse ($\phi = 0.53$) and ended it just before quadrature ($\phi = 0.73$). We note that our seeing-driven increase in exposure time adversely affected the quality of the spectra;

the exoplanet signal was subjected to “smearing,” a poorly documented phenomenon in which the exoplanet lines cross multiple resolution elements during an exposure, thus lowering the signal per resolution element. We discuss mitigation strategies for this “smearing” phenomenon in Section 3.

We simulated the model emission spectra of 55 Cnc e with the radiative-convective code HELIOS (Malik et al. 2019a, 2019b). We assume dayside-averaged conditions in radiative-convective equilibrium with no day-to-night heat transport, motivated by the strong day–night contrast measured by Mercier et al. (2022; $T_{\text{day}} = 3771^{+669}_{-520}$ K, $T_{\text{night}} < 1649$ K at 2σ) and by the short radiative timescales (versus advective transport timescales) expected for 55 Cnc e. The atmospheric surface pressure is set to 10 bar, in between previous estimates of ~ 1.4 –200 bar from the photometric/spectroscopic studies of Angelo & Hu (2017) and Bourrier et al. (2018), respectively.

We compute two model atmospheric grids using HELIOS. For the first grid, we calculated temperature–pressure profiles under bulk silicate earth (BSE) composition (Palme & O’Neill 2003; Ito et al. 2015) and under a Venus-like, CO₂-dominated atmosphere. The BSE composition with varying fractions of Fe (atmospheric mixing ratios of 0.1, 0.311, 0.537, and 1.0) is motivated by the potential for an evaporated mineral atmosphere in magma ocean planets (Schaefer & Fegley 2009; Miguel et al. 2011; Kite et al. 2016). Because the composition includes a high abundance of silicate species with strong optical absorption, this model produces a strong temperature inversion. In contrast, the Venusian atmosphere is motivated by expectations for a solid planet (Gaillard & Scaillet 2014), and its abundances produce a noninverted temperature–pressure structure. These temperature–pressure profiles were then postprocessed with varying Fe abundance, producing both pure-Fe and combined-species spectra based on the chemically consistent temperature–pressure profiles.

Our second model grid solely is based on initial BSE abundances. However, we here take the additional step of modeling atmosphere–magma ocean interaction as detailed in van Buchem et al. (2023) using an approach similar to that of MAGMA (Fegley & Cameron 1987; Schaefer & Fegley 2004) and of Ito et al. (2015). We assume chemical equilibrium between the magma and the overlying atmosphere, and the thermodynamics of the interior are modeled using the MELTS code (Ghiorso & Sack 1995). Assuming evenly mixed chemical profiles at the abundances produced by the atmosphere–magma ocean interaction at the dayside temperature of 55 Cnc e, we use HELIOS to postprocess temperature–pressure profiles computed assuming BSE abundances. Because we do

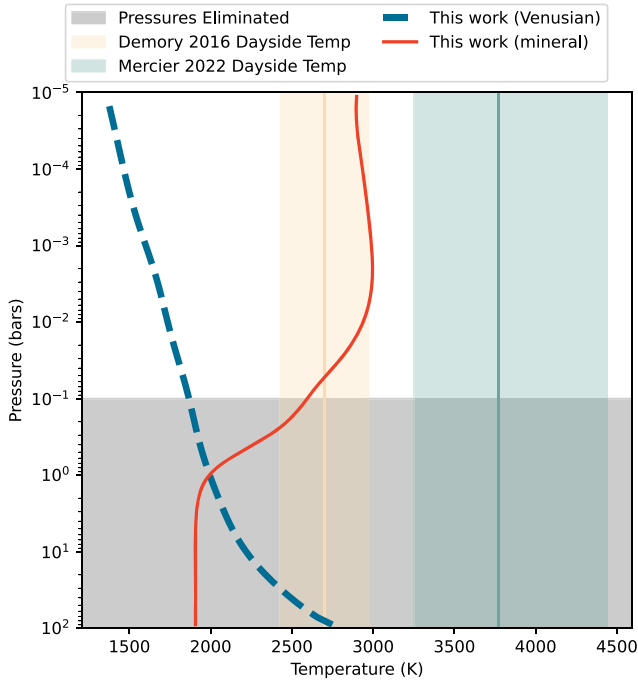


Figure 2. Temperature–pressure profiles used in this work from the HELIOS code (Malik et al. 2019a, 2019b). The Venusian models were not detected in any configuration of our injection tests.

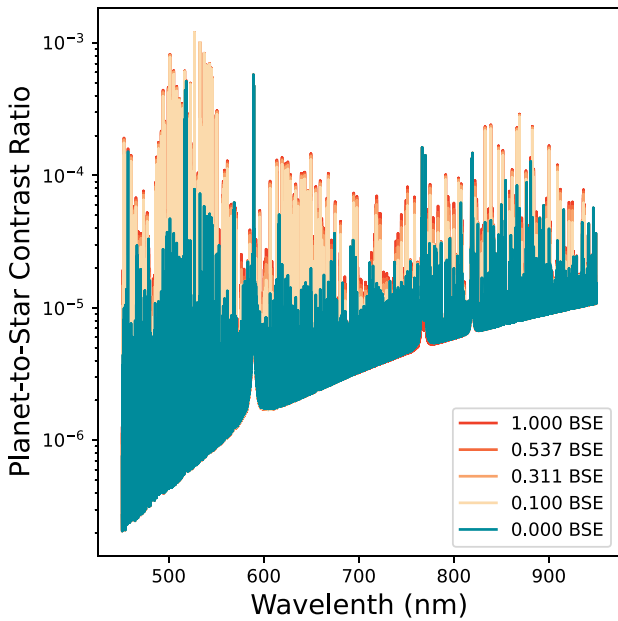


Figure 3. Model spectra for all species inclusive. The planet-to-star contrast ratio for all 10 bar atmospheres at varying fractions of Fe of bulk silicate Earth (BSE) is shown; all other abundances are held constant.

not compute vertical chemical abundances or link magma ocean output to atmospheric temperature–pressure profiles, we note that this method only provides an order-of-magnitude estimate for visibility in the high-resolution spectra. Additionally, we effectively vary the evenly mixed Fe abundance via the α_{Fe} parameter, as described in Putirka & Rarick (2019). All temperature–pressure profiles can be seen in Figure 2 and

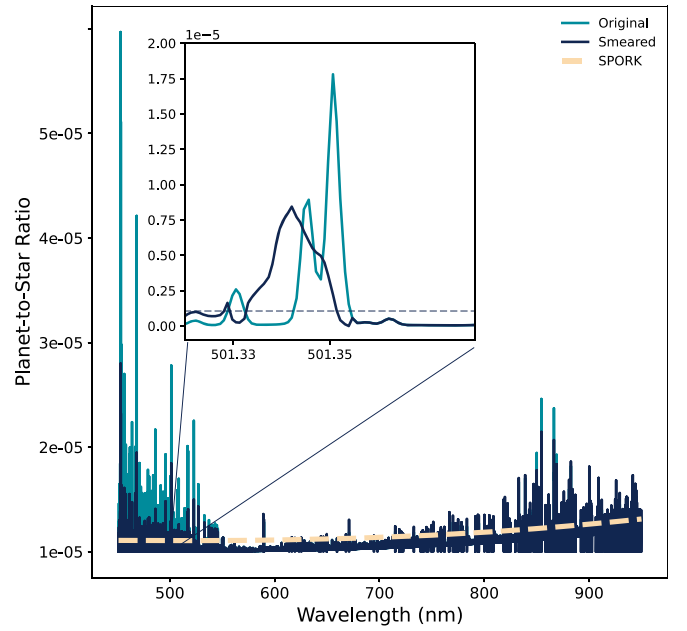


Figure 4. “Top hatting” of the model. The continuum is fit with the spline interpolating function SPORK (cream colored in the main panel, gray in the inset window) described in Rasmussen et al. (2022). The inset window shows an overlapping pair of emission lines which have been smeared out by the overlarge exposure time.

spectra for the combination of all species in a 10 bar atmosphere can be seen in Figure 3.

Convolving our model spectra with the Spitzer Channel 2 filter response function, we find an eclipse depth of 91 ppm for our 100% BSE model and 38 ppm for our Venusian model. Repeating this exercise in the CHEOPS band yields occultation depths of 5 ppm and 10 ppm for our BSE and Venusian models, respectively. While these models at first glance are discrepant from existing single Spitzer (Mercier et al. 2022) and CHEOPS (Demory et al. 2023) observed occultation depths of 209^{+50}_{-47} ppm and 12 ± 3 ppm, respectively, the models fall within the full range of observed variable occultations (Demory et al. 2016, 2023). In light of the lack of consensus on the observed variability’s origin, it is not immediately clear whether our models are constrained by existing photometric data. These values are 2.5σ and 3.6σ discrepant from the Mercier et al. (2022) analysis.

3. Methods

We use two established methods of exoplanet spectrum extraction to remove stellar and telluric lines. The principle behind both methods is the same: the exoplanet’s lines rapidly shift over resolution elements, while the star’s lines remain static to within one resolution element. Stationary features can thus be identified and removed via either principal component analysis (PCA; Thatte et al. 2010) or air mass detrending (Brogi & Line 2019).

Because telluric contamination is not significant in the optical, we simply remove the handful of orders in which H_2O and O_2 are present. We then run PCA or air mass detrending. For PCA, which can operate in either the wavelength (Zellem et al. 2014) or time regime (de Kok et al. 2013), common modes are identified between the input vectors and removed. The user can choose how many principal components are sufficient to maximize the detection of the exoplanet. For air

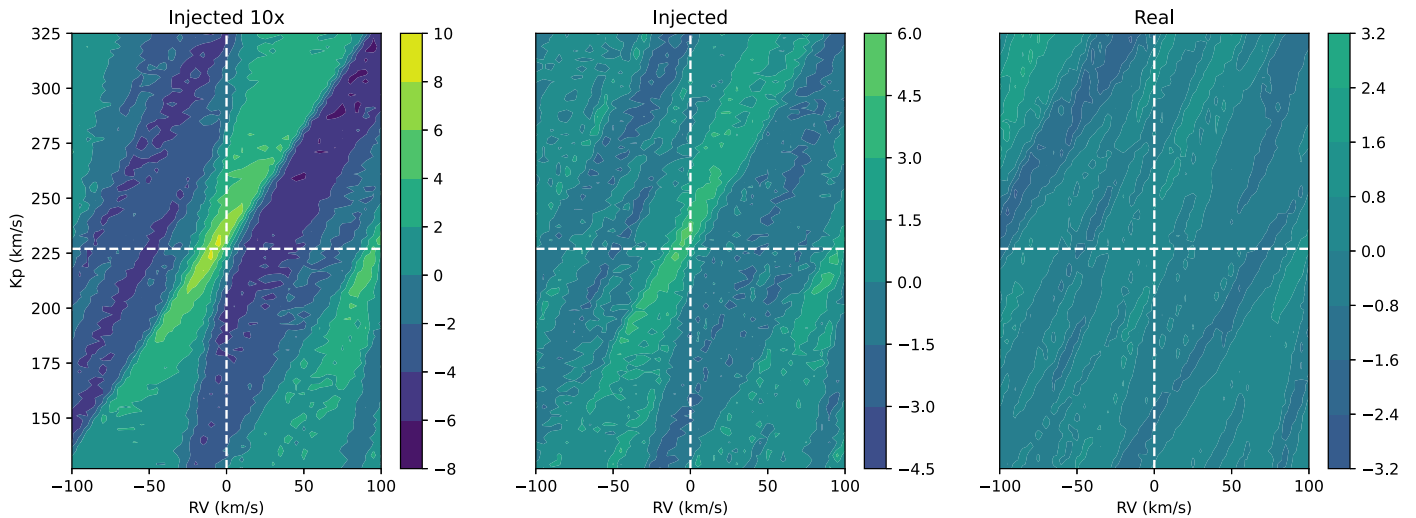


Figure 5. The noninverted 10 bar, 1.0 bulk silicate Earth (BSE) Fe atmosphere injection tests. (Left) The model is injected at 10 times the real contrast to illustrate where to expect the peak of the signal. The offset is due to the top-hatting (see Section 3) of the model which does not center the smeared lines but offsets them to the blue. (Center) The injected signal at the correct contrast is recovered at $\sim 6.0\sigma$. (Right) This model is not detected in the real data set.

mass detrending, the air mass trends of the spectrum are linearly fit and a median spectrum is divided out. This process is then repeated in the time domain.

The products of the telluric removal process are then cross-correlated against an unaltered $R \sim 100,000$ model spectrum, and the significance of that cross-correlation was assessed with the t-test method (Brogi & Line 2019) to generate detection significances. In the case of PCA, we test every iteration from one to seven principal components. For air mass detrending we test the standard method as well as the modified methods described in Rasmussen et al. (2022). To attempt to extract a signal from the spectra we use both methods with the understanding that to be robust, a significant cross-correlation peak at the expected planetary velocity should appear regardless of the method used.

We also perform injection tests to determine which species we should detect. We tested Mg, SiO, Na, K for the mineral models and H₂O and CO₂ for the Venusian models. We note that the orders with O₂ were not considered in this analysis due to significant telluric contamination, so an O₂ injection test was not performed. This is accomplished by injecting the model spectra into the real data and putting the result through the cross-correlation code. An important caveat of this process is that the observed exoplanet signal was subjected to significant smearing during the observation due to the need for longer exposure times due to suboptimal seeing conditions (see Section 2). The 300 s exposure times used in our observations were a factor of ~ 10 greater than the typical time it takes for an exoplanet spectral line to cross one resolution element, thus we expect the signal to be smeared across ~ 10 resolution elements.

We account for this smearing by “top hatting” the model before injection tests. In this method, lines are first identified by fitting the continuum of the emission spectra with the spline interpolation algorithm SPectral cOntinuum Refinement for telluriKs (SPORK; Rasmussen et al. 2022) and noting where features rise above it. The number of resolution elements crossed in the first exposure is then calculated from the change in radial velocity of the planet over time and the mean resolution of the spectrograph over its wavelength range using

the equation:

$$N_{\text{RE}} = R \frac{\Delta v}{c}, \quad (1)$$

where N_{RE} is the number of resolution elements crossed, Δv is the change in radial velocity, R is the resolving power of the instrument, and c is the speed of light.

Each identified feature is then smeared by dividing its height (H) by the number of resolution elements crossed (N_{RE}), and by adding that value to the next N_{RE} resolution elements. In this way the area under the emission line is conserved. A visualization of this process for a line-dense area of the spectrum is presented in Figure 4. We note a subtle difference in our “top-hatting” method compared to traditional boxcar smoothing: instead of smoothing equally about the center of a feature, our method smooths the signal toward shorter wavelengths, approximating smearing on the detector as the planet approaches quadrature. The top-hatted model is then used in our injection tests. Although the degree of smearing realistically differs from exposure to exposure, we use a constant smearing degree of 10 resolution elements (the maximum value), thus our estimate of our ability to recover the smeared signal is a conservative one. Finally, the injected data, after telluric removal, is cross-correlated against the unsmeared model.

4. Results and Discussion

We do not make any detections of any species in our data. We are, however, able to successfully rule out several scenarios. Iron is the only element which can be detected in our injection tests, so we focus on this element for our discussion. Comparison of our injection tests with the data, are able to rule out heavier ($P > 100$ mbar) BSE atmospheres to 4σ , but not lighter ones. We are also unable to recover any signal above 4σ from the Venusian injection tests. However, it is possible that, without the signal smearing the data experienced, we would be sensitive to lower pressures.

We perform injection tests for both our inverted and noninverted modeled atmospheres, and several different Fe abundances (atmospheric mixing ratios of 0.1, 0.311, 0.537,

and 1.0), and we are able to rule out all 100 mbar and 10 bar atmospheres at the 4–6 σ level, as these should have been detectable in the data. Atmospheric pressure has the largest impact on detection, with Fe abundance producing a secondary effect—for example, peak detection significance decreases from 5.29 σ to 3.82 σ for 10 bar 1 BSE to 10 bar 0.1 BSE. The 100 mbar atmospheres produces a 4.0 σ detection, which we regard as “tentative” and the boundary for detection. At atmospheric pressures below this, lower detection significances were obtained, which we deemed undetectable. An example of one of our injection tests is shown in Figure 5: we first increase the contrast of the model atmosphere by a factor of ten in order to see where to expect the peak of the signal (left); then we inject the planet at the real contrast ratio (center); and compare it to the injection-free data (right).

Mercier et al. (2022) claimed that a layer of emitting SiO is responsible for the high dayside temperature (3771 K) detected with the reanalysis of Spitzer phase curves. Despite the relatively high S/N of our data, we are unable to test this hypothesis due to the relatively weak features of that species at such a high temperature. Future observations compiled with this one may be able to confirm or refute this.

Two different Spitzer analyses have yielded two different brightness temperatures (\sim 2700 K from Demory et al. 2016 and \sim 3700 K from Mercier et al. 2022) for this planet. Demory et al. (2016)’s results are in line with our nondetections of Fe above $P = 100$ mbar (Figure 2). The latter proposes that strong emission from an SiO band may drive the high brightness temperature derived in the Spitzer 4.5 μ m data. Both analyses yield deeper eclipse depths for 55 Cnc e than both our BSE and our Venusian atmospheric models. If 55 Cnc e has an atmosphere, this may imply that it has stronger temperature inversion than our models can produce with this set of chemical abundances.

5. Conclusions

We have obtained the first high-resolution, high-S/N emission spectrum of 55 Cnc e to investigate the presence of a mineral atmosphere on this lava planet. Although we do not detect any species, injection tests reveal that an atmosphere which includes any abundance of Fe should be detected down to 100 mbar. We thus conclude that if this hot, close-in planet possesses any atmosphere at all, it is likely the product of weak crustal evaporation and below the detectability threshold of our ground-based data. 55 Cnc e is a Cycle 1 JWST target; space-based observations at low or medium resolution may be able to confirm our results.


















Acknowledgments

We thank our anonymous reviewer for their comments and suggestions that improved the clarity and robustness of the paper. K.C.R. and M.H.C. share co-first authorship. This work was performed by the Virtual Planetary Laboratory Team, a member of the NASA Nexus for Exoplanet System Science, funded via NASA Astrobiology Program grant No. 80NSSC18K0829. This research was also supported by grant No. 2019-1403 from the Heising-Simons Foundation.

ORCID iDs

Kaitlin C. Rasmussen  <https://orcid.org/0000-0002-0470-0800>

Miles H. Currie  <https://orcid.org/0000-0003-3429-4142>

Celeste Hagee  <https://orcid.org/0000-0001-7441-241X>
 Christiaan van Buchem  <https://orcid.org/0000-0001-8187-0312>
 Matej Malik  <https://orcid.org/0000-0002-2110-6694>
 Matteo Brogi  <https://orcid.org/0000-0002-7704-0153>
 Emily Rauscher  <https://orcid.org/0000-0003-3963-9672>
 Victoria Meadows  <https://orcid.org/0000-0002-1386-1710>
 Megan Mansfield  <https://orcid.org/0000-0003-4241-7413>
 Eliza M.-R. Kempton  <https://orcid.org/0000-0002-1337-9051>
 Jean-Michel Desert  <https://orcid.org/0000-0002-0875-8401>
 Joost P. Wardenier  <https://orcid.org/0000-0003-3191-2486>
 Lorenzo Pino  <https://orcid.org/0000-0002-1321-8856>
 Michael Line  <https://orcid.org/0000-0002-2338-476X>
 Vivien Parmentier  <https://orcid.org/0000-0001-9521-6258>
 Andreas Seifahrt  <https://orcid.org/0000-0003-4526-3747>
 David Kasper  <https://orcid.org/0000-0003-0534-6388>
 Madison Brady  <https://orcid.org/0000-0003-2404-2427>
 Jacob L. Bean  <https://orcid.org/0000-0003-4733-6532>

References

- Angelo, I., & Hu, R. 2017, *AJ*, 154, 232
 Bourrier, V., Dumusque, X., Dorn, C., et al. 2018, *A&A*, 619, A1
 Brogi, M., & Line, M. R. 2019, *AJ*, 157, 114
 Crida, A., Ligi, R., Dorn, C., & Lebreton, Y. 2018, *ApJ*, 860, 122
 de Kok, R. J., Brogi, M., Snellen, I. A. G., et al. 2013, *A&A*, 554, A82
 Deibert, E. K., de Mooij, E. J. W., Jayawardhana, R., et al. 2021, *AJ*, 161, 209
 Demory, B.-O., Gillon, M., de Wit, J., et al. 2016, *Natur*, 532, 207
 Demory, B.-O., Gillon, M., Madhusudhan, N., & Queloz, D. 2016, *MNRAS*, 455, 2018
 Demory, B. O., Sulis, S., Meier Valdés, E., et al. 2023, *A&A*, 669, A64
 Esteves, L. J., de Mooij, E. J. W., Jayawardhana, R., Watson, C., & de Kok, R. 2017, *AJ*, 153, 268
 Fegley, B., & Cameron, A. 1987, *E&PSL*, 82, 207
 Gaillard, F., & Scaillet, B. 2014, *E&PSL*, 403, 307
 Ghiorso, M. S., & Sack, R. O. 1995, *CoMP*, 119, 197
 Hammond, M., & Pierrehumbert, R. T. 2018, *ApJ*, 869, 65
 Ito, Y., Changeat, Q., Edwards, B., et al. 2022, *ExA*, 53, 357
 Ito, Y., Ikoma, M., Kawahara, H., et al. 2015, *ApJ*, 801, 144
 Jindal, A., de Mooij, E. J. W., Jayawardhana, R., et al. 2020, *AJ*, 160, 101
 Keles, E., Mallonn, M., Kitzmann, D., et al. 2022, *MNRAS*, 513, 1544
 Kite, E. S., Fegley, B., Jr., Schaefer, L., & Gaidos, E. 2016, *ApJ*, 828, 80
 Malik, M., Kempton, E. M. R., Koll, D. D. B., et al. 2019a, *ApJ*, 886, 142
 Malik, M., Kitzmann, D., Mendonça, J. M., et al. 2019b, *AJ*, 157, 170
 McArthur, B. E., Endl, M., Cochran, W. D., et al. 2004, *ApJL*, 614, L81
 Mercier, S. J., Dang, L., Gass, A., Cowan, N. B., & Bell, T. J. 2022, *AJ*, 164, 204
 Miguel, Y., Kaltenegger, L., Fegley, B., & Schaefer, L. 2011, *ApJL*, 742, L19
 Palme, H., & O’Neill, H. S. C. 2003, *TrGeo*, 2, 568
 Putirka, K. D., & Rarick, J. C. 2019, *AmMin*, 104, 817
 Rasmussen, K. C., Brogi, M., Rahman, F., et al. 2022, *AJ*, 164, 35
 Ridden-Harper, A. R., Snellen, I. A. G., Keller, C. U., et al. 2016, *A&A*, 593, A129
 Rucinski, S., Carroll, K., Kuschnig, R., Matthews, J., & Stibrany, P. 2003, *AdSpR*, 31, 371
 Schaefer, L., & Fegley, B. 2004, *Icar*, 169, 216
 Schaefer, L., & Fegley, B. 2009, *ApJL*, 703, L113
 Sulis, S., Dragomir, D., Lendl, M., et al. 2019, *A&A*, 631, A129
 Seifahrt, A., Bean, J. L., Stürmer, J., et al. 2016, *Proc. SPIE*, 9908, 990818
 Seifahrt, A., Stürmer, J., Bean, J. L., & Schwab, C. 2018, *Proc. SPIE*, 10702, 107026D
 Seifahrt, A., Bean, J. L., Stürmer, J., et al. 2020, *Proc. SPIE*, 11447, 114471F
 Seifahrt, A., Bean, J. L., Kasper, D., et al. 2022, *Proc. SPIE*, 12184, 121841G
 Thatte, A., Deroo, P., & Swain, M. R. 2010, *A&A*, 523, A35
 Tsiaras, A., Rocchetto, M., Waldmann, I. P., et al. 2016, *ApJ*, 820, 99
 van Buchem, C. P. A., Miguel, Y., Zilinskas, M., & van Westrenen, W. 2023, *M&PS*, 58, 1149
 Winn, J. N., Matthews, J. M., Dawson, R. I., et al. 2011, *ApJL*, 737, L18
 Zellem, R. T., Griffith, C. A., Deroo, P., Swain, M. R., & Waldmann, I. P. 2014, *ApJ*, 796, 48
 Zhang, M., Knutson, H. A., Wang, L., et al. 2021, *AJ*, 161, 181
 Zilinskas, M., van Buchem, C. P. A., Miguel, Y., et al. 2022, *A&A*, 661, A126